Nano Energy 90 (2021) 106600

Contents lists available at ScienceDirect

Nano Energy

journal homepage: www.elsevier.com/locate/nanoen

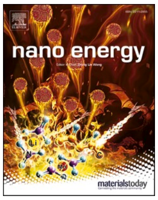

Ferroelectric-assisted high-performance triboelectric nanogenerators based on electrospun P(VDF-TrFE) composite nanofibers with barium titanate nanofillers

Guanbo Min [a,b], Abhilash Pullanchiyodan [b], Abhishek Singh Dahiya [b], Ensieh Seyed Hosseini [b], Yang Xu [a], Daniel M. Mulvihill [a], Ravinder Dahiya [b,*]

[a] *Materials and Manufacturing Research Group, James Watt School of Engineering, University of Glasgow, Glasgow G12 8QQ, UK*
[b] *Bendable Electronics and Sensing Technologies (BEST) Group, James Watt School of Engineering, University of Glasgow, Glasgow G12 8QQ, UK*

ARTICLE INFO

Keywords:
Electrospinning
PVDF-TrFE
BaTiO3
β-phase crystallinity
TENG

ABSTRACT

Triboelectric nanogenerators (TENGs) are flexible, efficient, and cost-effective energy harvesters. Here, we develop high-performance ferroelectric-assisted TENGs using electrospun fibrous surfaces based on P(VDF-TrFE) with dispersed $BaTiO_3$ (BTO) nanofillers in either cubic (CBTO) or tetragonal (TBTO) form. TENGs with three types of tribo-negative surface (pristine P(VDF-TrFE), P(VDF-TrFE)/CBTO and P(VDF-TrFE)/TBTO) in contact with PET were investigated and output increased progressively from pristine (0.75 W/m^2) to CBTO (2 W/m^2) and to TBTO (2.75 W/m^2). Accounting for contact pressure, the max output (V_{oc} = 315 V & J_{sc} = 6.7 $\mu A/cm^2$) is significantly higher than for TENGs having spin-coated P(VDF-TrFE)/BTO. It is hypothesized that electrospinning increases dipole alignment due to high applied voltages, but also aids the formation of a highly oriented crystalline β-phase via uniaxial stretching. Essentially, tribo-charge transfer is boosted due to increased surface potential owing to enhanced ferroelectric polarization. P(VDF-TrFE)/TBTO produced higher output than P(VDF-TrFE)/CBTO even though permittivity is nearly identical. Thus, it is shown that BTO fillers boost output, not just by increasing permittivity, but also by enhancing the crystallinity and amount of the β-phase (as TBTO produced a more crystalline β-phase present in greater amounts). Finally, the ferroelectric-assisted TENG was integrated with a flexible graphene electrode-based supercapacitor to produce a self-charging system capable of charging to 1.25 V in just 5 min. These results demonstrate that this technology can be valuable in wearable applications where higher power output, more efficient charging and flexibility are paramount.

1. Introduction

Energy autonomy of wearable electronic systems is a much-needed feature that has attracted considerable interest in recent years as reflected by the development of a wide variety of energy harvesters and storage devices [1–3]. Energy harvesters with flexible and/or stretchable form factors are the key element for the effective use of autonomous systems and have found application in a wide spectrum of areas such as: Internet-of-Things (IoT), wearable electronics, rehabilitation, respiration monitoring, actuation and motion sensing, air purification and gas sensing, and implantable biomedical devices [4–15]. One of the most promising energy harvesters is the triboelectric nanogenerator (TENG) – a technology that uses repeated or reciprocating contact of suitably chosen materials to generate charge via the triboelectric effect (TE) and utilizes this as usable voltage and current. TENGs are attractive as they can continuously generate charge over a wide range of operating conditions (i.e. forces and frequencies) [16,17] and have several valuable advantages such as light weight, simple structure, low cost and high efficiency at low frequencies [4, 5, 18–20]. TENGs have been explored in a wide range of applications, including self-powered wearable electronics/sensors, powering of flexible electronics and even for harvesting ocean wave/wind energy.

Many of these applications place demands on TENG materials such as: high flexibility, ability to maximize electrical output and robustness in sustaining high mechanical stress/strain [4, 21–24]. Several external approaches have been developed to maximize both output and usability: for example, an external charge pumping system was used in [25] to boost and regulate charge density at the electrodes and an external

---

* Corresponding author.
E-mail address: Ravinder.Dahiya@glasgow.ac.uk (R. Dahiya).

https://doi.org/10.1016/j.nanoen.2021.106600
Received 5 August 2021; Received in revised form 19 September 2021; Accepted 4 October 2021
Available online 8 October 2021

energy management system was developed in [26] to effectively utilize the low frequency power generated by TENGs. In terms of internally maximizing the electrical output of the TENG itself, a tribo-contact material pair that maximizes change transfer is required. Four key factors that help optimize this are maximizing: *real* contact area [27,28], difference in electron affinities of the interface pair [16], permittivity of the tribo-contact materials [29–31] and difference in residual surface potential between the interface surfaces [32,33]. With these demands in mind, materials that have received particular attention are the ferroelectric (FE) polymers polyvinylidene (PVDF) and copolymer poly (vinylidene fluoride-co-trifluoroethylene) (P(VDF-TrFE)) as these are flexible, but also allow for permanent polarization of the tribo-contact surfaces and are piezoelectric. Recent work has shown significant improvements (1–5 times) in TENG electrical output when polarized PVDF or P(VDF-TrFE) are compared to their non-polarized equivalent [32–34]. TENGs that also utilize the ferroelectric effect can be termed ferroelectric-assisted TENGs (or Fe-TENGs). Two approaches have been taken to fabrication: spin-coating [32,34–36,48,49] and electrospinning [37–44] – Table 1 compares output performance to date. The polar β-phase of these FE polymers is known for its exceptional piezoelectric (PE) properties (e.g., greatest degree of spontaneous polarization per unit cell [38,39]). To promote the β-phase formation, electrospinning is ideal as it combines uniaxial stretching and electric field poling in a single step [40,41,45]. The presence of aligned dipoles in the β-phase of FE polymers results in the enhancement of the spontaneous polarization and hence the surface charge density [34]. Recently, different material optimization routes have been followed to enhance the formation of the β-phase of FE polymers. For instance, it has been shown that addition of filler materials such as metal nanostructures, 2D materials and ceramic nanoparticles into the FE polymer matrix can enhance the formation of highly polar crystalline β-phase, because of the electrostatic interactions between the nanostructures and the highly aligned dipoles of the FE polymer chains [32,35,36,39,46]. The introduction of nanoparticles has another very important advantage i.e., high permittivity inorganic fillers can increase the dielectric constant of the tribo-contact materials, which serves to increase the TENG capacitance and hence the ability to store charge [30,32,36,47]. As an example, by dispersing particles of barium titanate (BTO with formula $BaTiO_3$) in a PVDF matrix, an increase in the open circuit voltage and short circuit current density of spin-coated TENGs by 1.5–2.4 and 1.8–2.3 times, respectively has been reported [36] (Table 1). Similarly, voltage and current increases of 1.6 and 1.5 times were observed with a similar dispersion of BTO particles in a P (VDF-TrFE) matrix [32]. Considering that TENGs produce high voltages but low currents, the current density is a vital parameter for performance. In this regard, using an electrospinning approach to create the P(VDF-TrFE)/BTO could provide better outcomes than methods such as spin-coating used in previous BTO work: electrospinning could enable even more highly charged P(VDF-TrFE)/BTO (nanofiber (NF) based) surfaces capable of further boosting current density. The premise is that electrospinning the P(VDF-TrFE)/BTO surface will lead to higher dipole alignment and crystallinity in the P(VDF-TrFE)/BTO matrix (due to higher voltage and extra alignment due to fiber stretching). Also, as TENG output increases with real contact area [27,28], there is another potential advantage to having a fibrous mat as one of the tribo-surfaces; namely, in certain cases, the flexible fibrous mat may be better able to conform to the topography of the opposing tribo-contact surface.

Table 1
Typical PVDF based TENG performances compared with the present work (final row).

Contact materials	Fabrication Method	Category	Pressure (kPa)	Freq. (Hz)	V_{oc} (V)	J_{sc} ($\mu A/cm^2$)	V_{oc}/Pressure (V/kPa)	J_{sc}/Pressure (μA/N)	Sample size cm^2	Ref.	
PVDF & Al	Electrospinning	Tribo	-	2	94.3	0.28	-	-	25	[27]	
PVDF-HFP & Silicon Rubber	Electrospinning	Tribo+piezo	20	1	17	0.06	0.85	0.03	4	[28]	
PVDF-AgNWs & Nylon	Electrospinning	Tribo+Piezo	12.5	3	240	3.0	19.2	2.46	4	[29]	
PVDF & CNF/PEI aerogel	Electrospinning	Tribo	30	10	105	4.5	3.5	1.5	2	[30]	
PVDF & Silk fibroin	Electrospinning	Tribo+piezo	32.1	4	500	1.5	15.6	0.47	8	[31]	
PVDF/MXene & PA6	Electrospinning	Tribo+piezo	25	1	50	2.5	2	1	4	[32]	
			125	4	300	15	2.4	1.2			
PVDF/Graphene & PA6	Electrospinning	Tribo+piezo	25	5	1373	14.1	54.9	5.64	4	[33]	
			225	5	1720	21.3	7.6	0.95	4		
PVDF/MXene & Nylon 11	Electrospinning	Tribo+piezo	23	4	75	3	3.3	1.3	3	[34]	
PDMS/BTO & Al	Spin-coating	Tribo+piezo	-	2	375	0.3	-	-	16	[37]	
PVDF & PVA	Spin-coating	Tribo	15	5	230	1.5	15.3	1	4	[38]	
P(VDF-TrFE) poled & Al	Spin-coating	Tribo+Ferro	380	5	10	4.0	0.03	0.11	1	[24]	
P(VDF-TrFE) & PET	Spin-coating	Tribo+piezo	-	0.5	35	0.6	-	-	1	[25]	
P(VDF-TrFE)/BTO poled & Al	Spin-coating	Tribo+ferro	98	-	45.7	1.25	0.47	0.13	1	[22]	BTO
PVDF-BTO & PA6	Spin-coating	Tribo+piezo	250	5	450	3.2	1.8	0.13	4	[26]	
P(VDF-TrFE)/BTO & PET	**Electrospinning**	**Tribo+ferro**	**12.8**	**4**	**315**	**6.7**	**24.6**	**5.23**	**6.25**	**This work**	

Therefore, in this work, high-performance ferroelectric-assisted TENGs using electrospun fibrous tribo-negative surfaces based on P(VDF-TrFE) composites with dispersed $BaTiO_3$ (BTO) nanofillers have been developed. We also explored the use of cubic BTO (CBTO) as a means of probing the differences introduced by the piezoelectric tetragonal BTO (TBTO) as compared to the non-piezoelectric CBTO and this has led to interesting new conclusions about the mechanisms by which BTO fillers boost performance (i.e., the importance of the amount and level of β-phase crystallinity in boosting performance). Accordingly, three types of β-phase crystalline P(VDF-TrFE) NF-based mats were fabricated (via electrospinning) as active negative TE layers: pristine P(VDF-TrFE), P(VDF-TrFE)/CBTO and P(VDF-TrFE)/TBTO. PET sheet material was used as the positive tribo-layer in all three cases to complete the Fe-TENGs. TENG output increases monotonically with contact pressure [27,28], so it is important to take account of the contact pressure used in TENG measurements as various labs generally publish results at different pressures. For this reason, we have also included the open circuit voltage per unit pressure and short circuit current density per unit pressure in Table 1 (units of V/kPa and μA/N, respectively – i.e., the voltages and currents are just divided by the applicable nominal average contact pressure). Looking at the pressure normalized values of open circuit voltage and short circuit current density, we see that the present electrospun work at 24.6 V/kPa and 5.23 μA/N is a considerable advance over the previous spin-coating work on PVDF/BTO [36] (i.e. 1.8 V/kPa and 0.13 μA/N) and P(VDF-TrFE)/BTO [32] (i.e. 0.47 V/kPa and 0.13 0.13 μA/N). There is only one result in Table 1 that has exceeded our output performance; namely Ref. [43] who achieved an open circuit voltage per unit pressure of 54.9 V/kPa and a short circuit current density per unit pressure of 5.6 μA/N. However, the result in [43] was achieved with a very different material combination: a tribo-negative surface based on graphene sheets dispersed in a PVDF matrix and a Nylon 6 tribo-positive surface. There, the enhancement mechanism with graphene sheets is rather different to that with BTO and Nylon 6 is also considerably more tribo-positive than the PET used in this work. As a final step, we integrated the Fe-TENGs (P(VDF-TrFE)/TBTO) with a graphene electrode based flexible supercapacitor to realize a self-charging system that can charge to 1.25 V in just 5 min.

2. Experiments

2.1. Preparation of materials

The fibrous (electronegative) surfaces were electrospun from three different solutions: pure P(VDF-TrFE) (Piezotech, France), P(VDF-TrFE) mixed with cubic $BaTiO_3$ (CBTO, Sigma-Aldrich, UK), and tetragonal $BaTiO_3$ (TBTO, Sigma-Aldrich, UK) powders. The fabrication steps for the P(VDF-TrFE), P(VDF-TrFE)/CBTO and P(VDF-TrFE)/TBTO solutions are illustrated in Fig. 1. A 15 wt% P(VDF-TrFE) solution was prepared by dissolving P(VDF-TrFE) powder in a DMF and acetone (Sigma-Aldrich, UK) mixed solvent (1:1 ratio) for 10 h under stirring by a magnetic stir bar at 300 rpm and 25℃ (Fig. 1a). The resulting solution was stirred until the solution is homogeneous and completely transparent. P(VDF-TrFE) and BTO composite solutions were prepared by mixing CBTO or TBTO with the resulting P(VDF-TrFE) solution at 3 wt% (Fig. 1b,c). Note, 3 wt% was chosen as this led to optimum voltage and current output (See Fig. S1 in Supplementary Information). The nanocomposite solutions were then stirred at 300 rpm at 25℃ for 4 h to disperse the CBTO or TBTO in the P(VDF-TrFE) solution uniformly and form the P(VDF-TrFE)/CBTO and P(VDF-TrFE)/TBTO slurry.

2.2. Electrospinning

Electrospinning of the NFs was conducted using an electrospinning machine. The prepared solutions were filled into a 10 mL syringe and connected to a spinneret with a 21 G-gauge needle. After that, the electrospinning of solution was executed at a high voltage of 17 kV and a flow rate of 0.5 mL/h with a 15 cm distance between the needle and

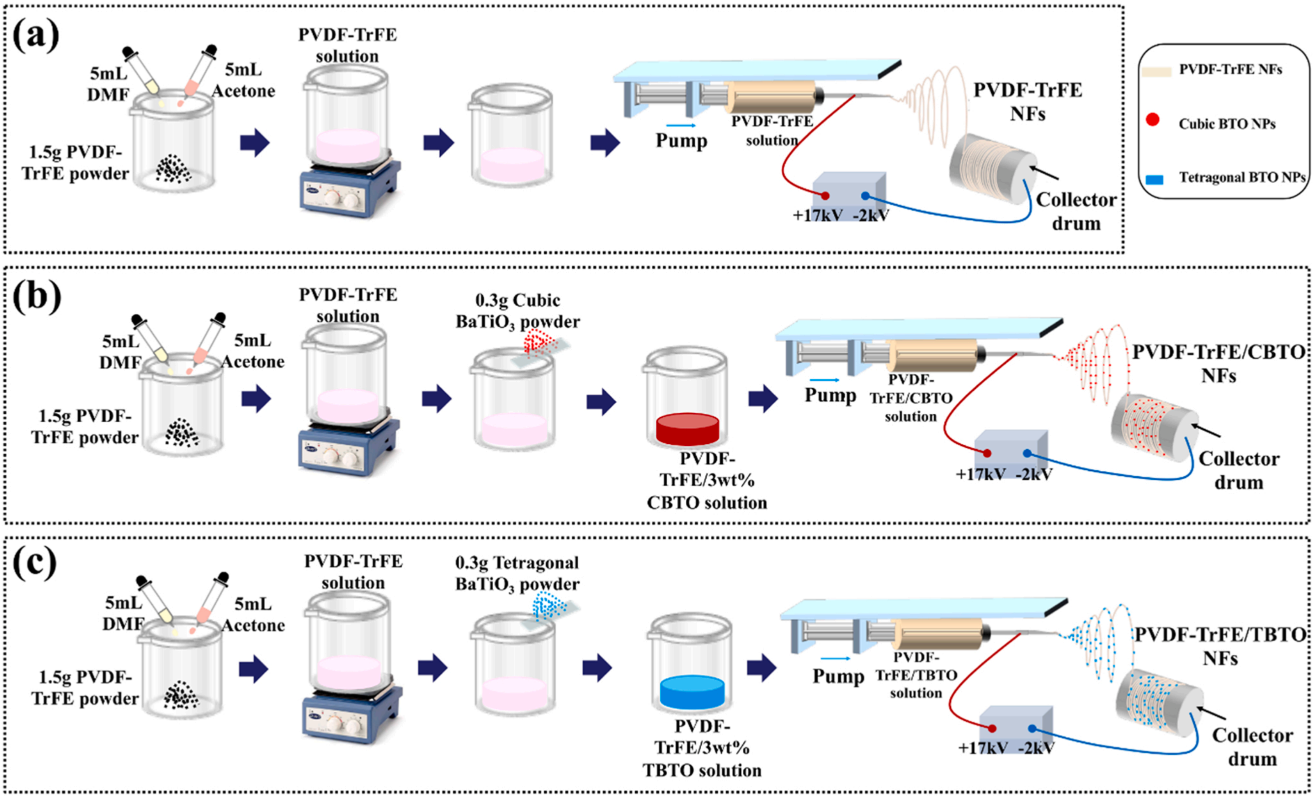

Fig. 1. Fabrication procedures for (a) P(VDF-TrFE), (b) P(VDF-TrFE)/CBTO and (c) P(VDF-TrFE)/TBTO NF mats by electrospinning.

drum collector, as shown in Fig. 1a–c. The electrospun NFs were collected by a drum collector, which was covered by an aluminum foil (Sigma-Aldrich, UK), with a 2 kV voltage rotating at 1500 rpm. All three polymer solutions (P(VDF-TrFE), P(VDF-TrFE)/CBTO and P(VDF-TrFE)/TBTO NFs) were electrospun using the same fabrication parameters at room temperature and humidity. Note, achieving optimum electrospinning parameters for this application is not straightforward as formation of β-phase P(VDF-TrFE) (critical for enabling higher polarization) is sensitive to several parameters including voltage, concentration of P(VDF-TrFE), viscosity and distance between needle and collector. To have NF mats with similar thicknesses, each of the three NF mats were collected on the Al foil for around 2 h which produced nanofiber mats with thickness of about $8\mu m$ (see Fig. S2 for surface profiles indicating thickness). The electrospun NF mats covering the Al foil were then cut into small pieces (4×2.5 cm^2) as shown in Fig. S3 and used as the negative tribo-layer. A fixed ITO coated Polyethylene terephthalate (PET) film (4×2.5 cm^2, Sigma-Aldrich, UK) with a resistivity of 60 Ω/sq and 0.127 mm thickness was used as the positive tribo-layer for each of the three sample types (to keep the counter-surface material constant). To avoid a bulge from the electrode lead wires interfering with the contact area, the interface pair positioning was mismatched at a fixed nominal contact area of 2.5×2.5 cm^2 during the measurements (i.e., to allow a free region for attachment of the wires). To measure the pure piezoelectric response, the P(VDF-TrFE)/TBTO nanofiber-based mat was sandwiched between two Al electrodes and encapsulated with a polyimide tape as shown in Fig. S4.

2.3. Characterization and testing

X-ray diffraction (XRD), employing a PANalytical X‘Pert Pro diffractometer with a Cu Kα source ($\lambda = 1.541$ Å) was used to characterize crystallinity and the $\beta-$phase in the P(VDF-TrFE) matrix for each of the three varieties of electrospun NFs. The surface topography of electrospun NFs and PET surface was measured prior to testing by an optical 3D surface profilometer (Alicona, InfiniteFocus) and an atomic force microscope (AFM) (Dimension Icon, Bruker). Scanning electron microscopy (SEM) was used to describe the surface structure and morphology of the electrospun NF mats.

The rig used for TENG testing (normal contact separation mode) is the same as explained elsewhere [27]. Prior to testing, a pre-load was applied to make contact and to self-align the surfaces. The alignment is then ‘locked-in’ by tightening lock screws. The mechanical oscillation for the TENGs was supplied by an oscillating force (8 N with 4 Hz frequency) using an electrodynamic shaker system (TIRA, TV 50018, Germany). This produces a corresponding nominal contact pressure of 12.8kPa. Mechanical oscillation was configured with a 2 mm max separation distance (i.e., peak-to-peak amplitude of 2 mm). A 5 min pre-charge time is employed before each set of measurements to ensure equilibrium of tribo-charge generation. The output voltage was recorded by an oscilloscope (MSO-X 4154A, KEYSIGHT, USA) connected to an operational amplifier and a voltage divider circuit to ensure that the impedance of the voltage meter setup was much larger than the TENG internal impedance (See Fig. S5a for details). Simultaneously, the oscilloscope was also coupled with an inverting current to voltage converter which consisted of a 100 kΩ feedback resistor and a LMC6001 operational amplifier (ultra-input current amplifier) to measure the output current in Fig. S5b [50]. When comparing the three TENG devices with the different tribo-negative surfaces (and when testing with different resistive loads) all test parameters (contact pressure, frequency, separation distance etc.) were maintained constant.

2.4. Graphene supercapacitor

To demonstrate the self-charging capability of the developed Fe-TENGs, a flexible supercapacitor (FSC) was fabricated using multilayer graphene sheets (GS, Graphene Supermarket, USA) based on our previous report [51]. In a typical process, the GS film having an area of 3 cm^2 was used as the current collector and electrode material. At first, the GS film was pasted on flexible polyethylene terephthalate (PET) substrates by polyurethane (PU) resin as the binder. A conducting metal wire was fixed on top of the graphene sheet by silver (Ag) conductive epoxy (RS components, 186-3600) for the external connection and insulated with PU coating and dried for 2 h at 80℃ in a hot air oven. Polyvinyl alcohol (PVA)-phosphoric acid (H_3PO_4) based gel electrolyte was used for the FSC fabrication. The preparation of the gel electrolyte was reported in our previous work [52]. Herein, first we dissolved the PVA (10 wt%) in hot water with continuous stirring followed by the addition of H_3PO_4. A polyester/cellulose blend (Techni Cloth, TX 612) was used as a separator. A schematic representation of the fabricated FSC is shown in Fig. 7a. To charge the supercapacitor, the Fe-TENGs and supercapacitor were coupled by a rectifier circuit which consists of four diodes as shown in Fig. 7b.

3. Result and discussion

3.1. TENG performance

Fig. 2a–c illustrate the structure of the three TENG devices under investigation having the tribo-negative material as pristine P(VDF-TrFE), P(VDF-TrFE)/CBTO composite or P(VDF-TrFE)/TBTO composite (each in contact with PET). Note: bound charges and tribocharges are also illustrated here to aid the discussion below. Device output is characterized in Fig. 2d–i. Fig. 2d and e compare voltages and current densities for each of the three devices at open circuit and short circuit conditions, respectively. Both outputs increase as we move from the pristine P(VDF-TrFE) case to P(VDF-TrFE)/CBTO and to P(VDF-TrFE)/TBTO. The peak positive open circuit voltage V_{oc} increased from 225 V (pristine) to 293 V (P(VDF-TrFE)/CBTO) and to 315 V (P(VDF-TrFE)/TBTO), i.e., 1.4 times increase from pristine to P(VDF-TrFE)/TBTO. These voltages are comparable with previous work (Table 1). TENGs are high voltage but low current devices and a critical requirement therefore is to boost the current density. In Fig. 2e, the peak short circuit current density was about 1.95 μA/cm^2 for the pristine case, 5.5 μA/cm^2 for P(VDF-TrFE)/CBTO and a maximum of 6.7 μA/cm^2 for P(VDF-TrFE)/TBTO representing an increase of 3.4 times over the pristine case. Additionally, A similar trend is seen in Fig. S6 for the transferred charges. The comparison of our result with previous work on similar materials is given in Table 1. For example, with a PVDF-TBTO based device in contact with PA6 in [36] and a P(VDF-TrFE)/TBTO based device in contact with Aluminum in [32]. The former achieved a maximum current density of 3.2 μA/cm^2 at a contact pressure of 250 kPa and the latter reported a maximum of 1.25 μA/cm^2 at a contact pressure of 98 kPa. The present work has produced significantly higher current density (6.7 μA/cm^2) at much lower contact pressure of only 12.8 kPa. Interestingly, these gains are possible with the counter surface (PET), which is far less tribo-positive than the tribo-positive materials used in above mentioned previous works. In fact, 6.7 μA/cm^2 is among the highest value in Table 1 where the present work is compared to related work in the literature (i.e. where similar materials were used). The contact pressure is an important factor here as TENG output increases significantly with contact pressure. Therefore, this marked boosting of the current density could be largely attributed to the effect of the electrospinning process used here as previous works used spin-coated films with [32] and without [36] electrical poling. Specifically, the electrospinning here used a higher voltage (17 kV) compared to the poling used in [32] (8 kV). To illustrate this, we have compared our electrospun results to those from equivalent DC poled spin coated films. The output voltage of the device fabricated by electrospun P(VDF-TrFE)/TBTO is 2.1 times higher than the equivalent poled PVDF-TrFE/TBTO device in Fig. S7b (a similar result is evident in Fig. S7a for pristine P(VDF-TrFE)). The higher voltage in electrospinning is likely to encourage enhanced dipole alignment in the P(VDF-TrFE) matrix. Also, uniaxial fiber

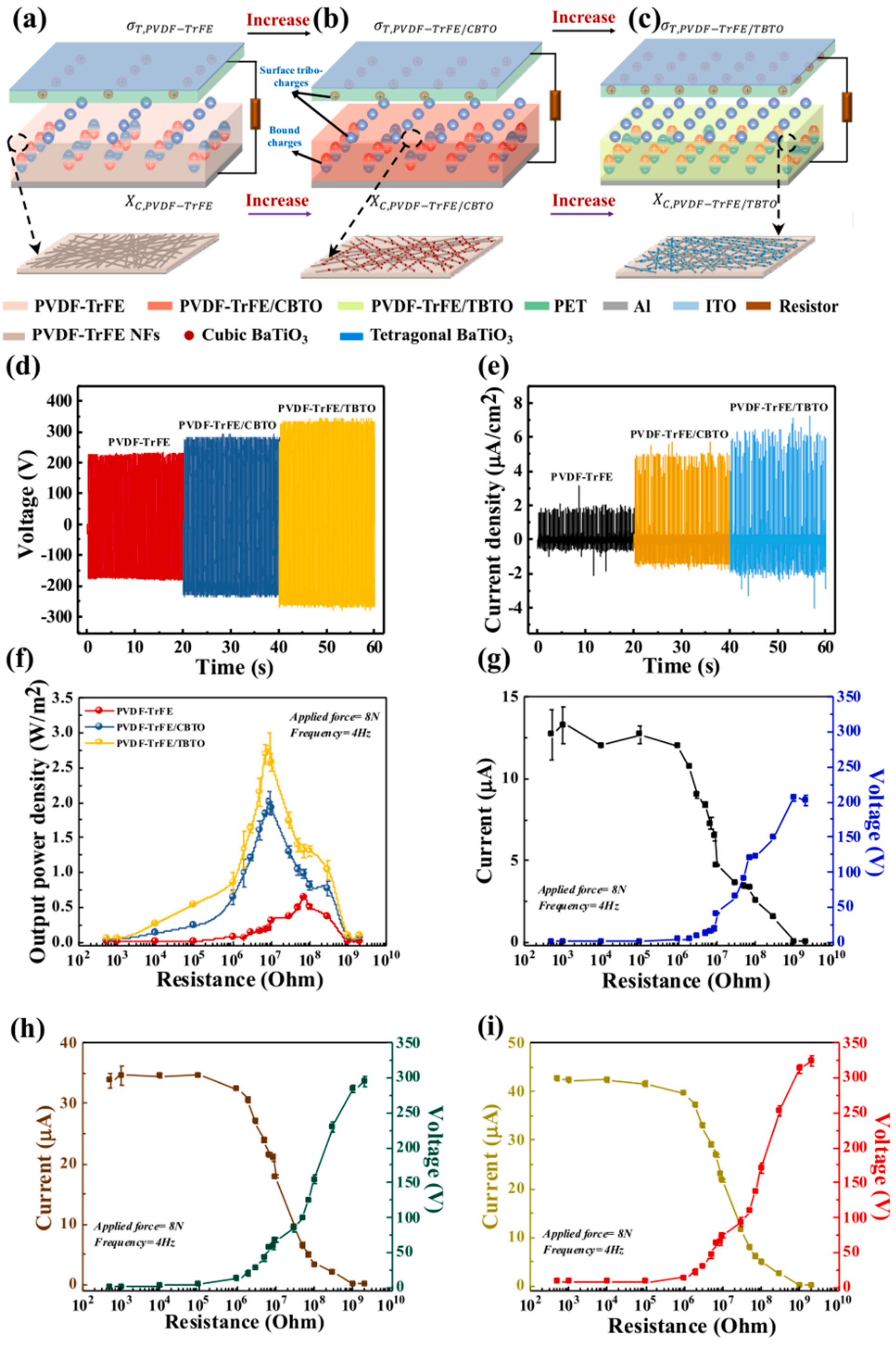

Fig. 2. Characterization of device performance. (a–c) Illustrate Fe-TENG device structure having negative tribo-surface as: (a) P(VDF-TrFE), (b) P(VDF-TrFE)/CBTO and (c) P(VDF-TrFE)/TBTO (with PET at the positive tribo-layer in each case). (a–c) Also illustrate the role of ferroelectric polarization in affecting the triboelectric surface potential and charge density by indicating how the bias of the bound charges and the level of tribocharges increases as we move to P(VDF-TrFE)/TBTO (Note: X_C is degree of crystallinity & σ_T is tribocharge density). Electrical output is characterized in (d–i) for each of the three device types as follows: (d) open circuit voltage, (e) short circuit current density, (f) output power density and (g–i) output current and voltage versus resistive load for (g) pristine P(VDF-TrFE) & PET, (h) P(VDF-TrFE)/CBTO & PET and (i) P(VDF-TrFE)/TBTO & PET. Contact pressure was fixed at 12.8 kPa.

stretching during the electrospinning process is likely to result in more highly aligned, more crystalline P(VDF-TrFE). These effects are likely to confer higher surface polarity (i.e., higher surface potential) and enable a further boosting of triboelectric charge transfer leading to the higher currents observed. Electrospinning also has the advantage of eliminating the extra poling step as this is now a seamless part of the process. Output power is plotted against resistive load in Fig. 2f and the corresponding plots of voltage and current versus resistance are shown in Fig. 2g–i. Energy harvesting devices such as TENGs generally present high internal impedance to load circuits and in general, the maximum output power is obtained when the load impedance is matched to that of the harvester. Across the three TENG device variants here, the optimum power occurs in the resistance range of 100–500 MΩ. Following the voltage and current trend, peak power increased from about 0.75 W/m^2 for the pristine P(VDF-TrFE) to about 2 W/m^2 for P(VDF-TrFE)/CBTO and 2.75 W/m^2 for P(VDF-TrFE)/TBTO - thus representing 3.2 times increase over the pristine case. The developed Fe-TENG retained approximately 95% of the original output voltage in Fig. 2i after 10,000 cycles of repeated vibration, as shown in Fig. S8 – thus the device exhibits good stability.

Analyzing the intrinsic properties of the three negative tribo-layer materials can help trace the source of the output differences between the three cases and improve our understanding of the underlying behavior. It has been shown that the intrinsic properties of P(VDF-TrFE) NFs govern the output performance of TENGs. This is because the surface potential of the contact layer is correlated with the degree of crystallinity of the β-phase of the P(VDF-TrFE) NFs [39,53,54]. To probe the crystallinity of the NFs, X-ray diffraction (XRD) measurements were performed on all three categories of P(VDF-TrFE) and its composite NF samples (results are shown in Fig. 3a). From the XRD data, we can see a dominant peak centered at $2\theta = 19.96^\circ$ for all three samples, corresponding to the reflection of the crystalline β-phase (110/200) of P (VDF-TrFE). It is important to note that none of the samples showed the non-polar α phase (present at 2θ = 18.3). These results also suggest good dispersion of BTO nanoparticles in the P(VDF-TrFE) matrix. Among the three phases of P(VDF-TrFE) namely, alpha, beta and gamma, the β-phase can generate highest surface tribo-charge density because it provides the highest dipolar moment per unit cell (i.e. surface dipole moment) [55,56]. The characteristic diffraction peak of BTO nanoparticles at $2\theta = 22.2^\circ$ is also apparent in Fig. 3a for the P (VDF-TrFE) composite NFs (in blue for TBTO and black for CBTO). In theory, the XRD diffraction of the tetragonal BTO show peak splitting at 22.2° corresponding to the (hkl) Miller index (001) and (100), whereas cubic BTO would have a single peak corresponding to (002) [57]. The P (VDF-TrFE)/TBTO NFs diffraction pattern (blue line) exhibits typical characteristics of tetragonal BTO (peak splitting at 22.2°) with a single peak at $2\theta = 22.2^\circ$ for the CBTO sample. The cubic phase of BTO belongs to the centrosymmetric crystal class m3m and thus, is non-piezoelectric [58].

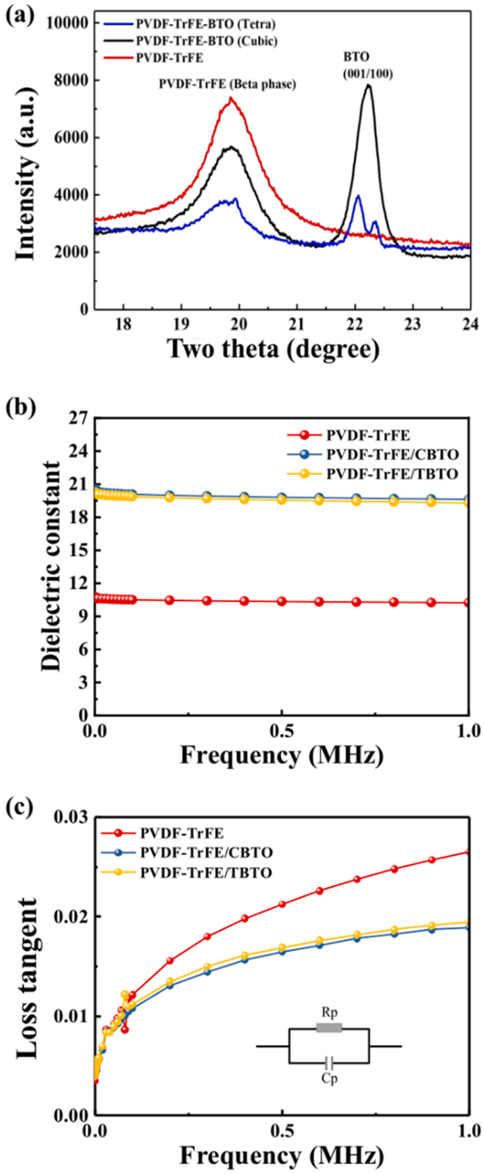

Fig. 3. Materials characterization for P(VDF-TrFE) and P(VDF-TrFE)/BTO: (a) X-ray diffraction (XRD) results of P(VDF-TrFE) (red line), P(VDF-TrFE)/CBTO (black line) and P(VDF-TrFE)/TBTO (blue line) with crystalline β-phase (110/200) and XRD patterns of the cubic and tetragonal BTO nanoparticles (001/100); (b) as-measured dielectric properties of the nano-fibrous mats for: P(VDF-TrFE), P(VDF-TrFE)/CBTO, and P(VDF-TrFE)/ TBTO. Note: there is little difference in permittivity between CBTO and TBTO nanofillers meaning that permittivity cannot explain the TENG output boost with TBTO and (c) as-measured tangent loss of the nanofibrous mats for: P(VDF-TrFE), P(VDF-TrFE)/CBTO and P(VDF-TrFE)/TBTO.

Exploring both CBTO and TBTO in the same work allows us to probe the underlying behavior further. We noted from Fig. 2, that voltage, current and power increase progressively as we move from pristine P (VDF-TrFE) to P(VDF-TrFE)/CBTO to P(VDF-TrFE)/TBTO. For example, the current density increases 2.8 times in going from the pristine case to P(VDF-TrFE)/CBTO. If we then go to P(VDF-TrFE)/ TBTO, we notice a further boosting of output to 3.4 times the pristine case. To explain the increases attributable to the BTO nanofillers, there are two key mechanisms: the first (well outlined in [32] and [36]) is that the addition of high permittivity fillers (i.e. the CBTO) dramatically increases the permittivity of the resulting P(VDF-TrFE)/BTO matrix (for example, a factor of 6–7 increase in permittivity is reported after addition of CBTO nanofillers to P(VDF-TrFE) [59]). Higher permittivity contact materials increase TENG capacitance, thereby increasing the ability to induce and store more tribo-charge and drive higher currents. Permittivity measurements for the three nano-fibrous mat types in this work are given in Fig. 3b. The results show the expected boost in permittivity due to the BTO fillers and confirm that CBTO and TBTO result in near identical permittivity values. Therefore, to explain the higher TENG output with TBTO (compared to CBTO), we turn to the second reason and the one we would like to focus on more in this paper.

In a recent work on piezoelectric sensors, the addition of CBTO nanofillers into a P(VDF-TrFE) matrix has been noted to significantly boost β-phase crystallinity by becoming advantageous nucleation sites for the crystalline β-phase [60]. This therefore increased residual polarity and piezoelectric coefficient. Here we explore this role of the BTO nanofillers in increasing crystallinity and how this might be advantageous in the TENG context. The crystalline quality is a parameter that can be determined by calculating the full width at half maximum (FWHM) [61]. Note, a smaller value of FWHM corresponds to the higher β-phase crystallinity. We calculated the FWHM values for pristine P (VDF-TrFE), P(VDF-TrFE)/CBTO and P(VDF-TrFE)/TBTO NFs and these are 0.95, 0.89 and 0.81, respectively. Based on these results, the P (VDF-TrFE)/TBTO NFs have highest crystallinity among the three electrospun materials. We also noted via FTIR Spectroscopy analysis of the P (VDF-TrFE)/BTO that the amount of β-phase was higher for TBTO nanofillers (67%) than for CBTO (54%) – See Supplementary Information and Fig. S9. The existence of β-phase with higher crystallinity and in higher proportions will improve dipole alignment and polarization in the P(VDF-TrFE)/BTO matrix leading to an increase in the surface potential of the tribo-negative contact material. Estimates of surface potential outlined in the Supplementary Information follow this trend. Estimated surface potential for pristine P(VDF-TrFE) was 133 V and this increased to 189 V with addition of CBTO fillers and was further boosted to 214 V for TBTO fillers (see Fig. S10). As noted, the extra output available with the TBTO nanofillers (compared with CBTO nanofillers) seems to be entirely attributable to the crystallinity effect (as both P (VDF-TrFE)/CBTO and P(VDF-TrFE)/TBTO produce very similar permittivity – Fig. 3b). We can thus conclude that, in both cases (CBTO and TBTO nanofillers), the TENG enhancement mechanism is a combination of enhancing both permittivity and β-phase crystallinity.

The loss tangent for P(VDF-TrFE)/TBTO, P(VDF-TrFE)/CBTO and P (VDF-TrFE) has been calculated by using: $\tan\delta = \frac{1}{2\pi f C_p R_p}$. Note, the C_p

and R_p were tested using a LCR meter (Keysight E4980, UK). They are the parallel mode capacitance and resistance of sample as illustrated in Fig. 3c. The loss tangent is lower in the P(VDF-TrFE)/BTO composites compared with the pristine P(VDF-TrFE), especially at the higher frequencies in Fig. 3c, because of the glass transition relaxation of the PVDF-TrFE polymer matrix [62,63]. However, the loss tangent of P(VDF-TrFE)/ TBTO and P(VDF-TrFE)/ CBTO result in near identical values.

To fully understand how enhanced residual polarization of the P(VDF-TrFE) and its composites boosts TENG output, it is useful to refer to the overlapped electron-cloud (OEC) model [33,64]. This model describes the process of intrinsic electron transfer between two contact materials. Using the OEC model, Fig. 4 schematically illustrates the electron transfer process when each of the three tribo-negative materials are pressed into contact with the tribo-positive PET. In Fig. 4, $E_{F,\ P(VDF\text{-}TrFE)}$, $E_{F,\ P(VDF\text{-}TrFE)/CBTO}$ and $E_{F,\ P(VDF\text{-}TrFE)/TBTO}$ represent the Fermi levels of P(VDF-TrFE), P(VDF-TrFE)/CBTO and P(VDF-TrFE)/TBTO, respectively and the greatest energy level difference between these surfaces and PET are represented by ΔE, ΔE′ and ΔE′′, respectively.

P(VDF-TrFE) and its composites play the role of the tribo-negative material, accepting electrons from PET during contact electrification. The combination of polarization due to electrospinning and due to enhancements in crystallinity is likely to lead to high dipole alignment resulting in high surface potential. Simultaneously, the presence of bound charges, generated by aligned dipoles, will boost the potential energy [53]. As confirmed by the XRD scans, the P(VDF-TrFE)/TBTO sample has shown higher crystallinity than P(VDF-TrFE)/CBTO and P(VDF-TrFE)/CBTO has shown better crystallinity than pristine P(VDF-TrFE). Accordingly, as shown in Fig. 4, the Fermi levels should be in order of $E_{F,\ P(VDF\text{-}TrFE)} > E_{F,\ P(VDF\text{-}TrFE)/CBTO} > E_{F,\ P(VDF\text{-}TrFE)/TBTO}$. As shown in Fig. 4a, when the PET is not in contact with pristine P(VDF-TrFE) NFs, the electron clouds of the materials do not overlap and there is negligible electron transfer between the two atoms. When contact occurs, the potential barrier between them (ΔE) decreases, and the electrons can transfer between the two atoms until their Fermi levels are in equilibrium (i.e. until $E'_{F,PET} = E'_{F,PVDF-TrFE}$). After incorporating the CBTO/TBTO nanoparticles into the P(VDF-TrFE) matrix, the Fermi level of the negative tribo-layer can be expected to shift downwards due to enhanced surface polarization. As the Fermi level of the PET sheet ($E_{F,PET}$) is fixed in each case, the energy difference is in the following order: ΔE < ΔE′ < ΔE′′. A greater difference in energy levels means more empty surface states of the negative tribo-layer can be filled with electrons from the PET surface (due to the increased differences in work function between the contact materials) and hence higher tribo-charge transfer. After separating the interface pair, the tribo-charge density of a dielectric-dielectric TENG is given by [65]:

$$\sigma_T = \frac{e(\varphi_2 - \varphi_1)}{\frac{1}{N_{s1}} + \frac{1}{N_{s2}} + \frac{2e^2x_0}{\varepsilon_0}} \tag{1}$$

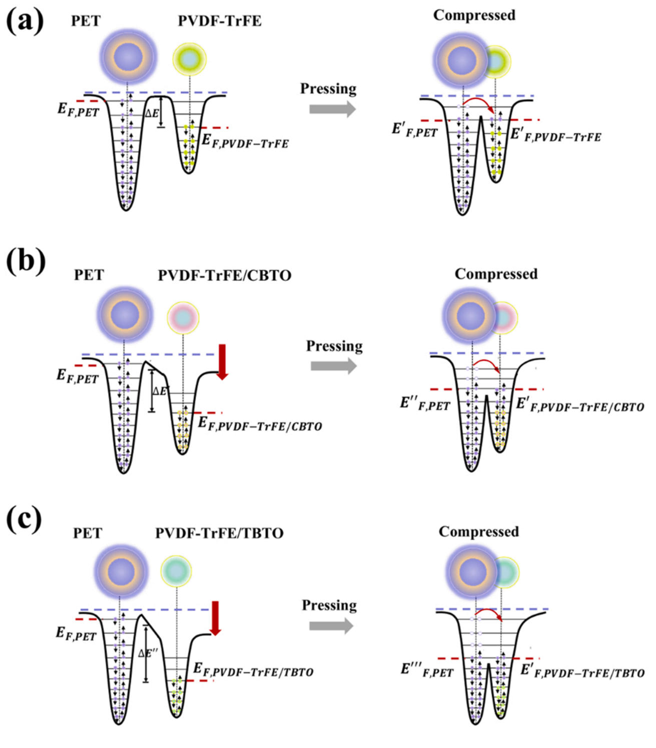

Fig. 4. (a) Overlapped electron cloud (OEC) model of electron transfer between interface pairs for (a) P(VDF-TrFE) & PET, (b) P(VDF-TrFE)/CBTO & PET and (c) P(VDF-TrFE)/TBTO & PET as adapted from [33,64].

Where, $\varphi_{1,2}$ and $N_{s1,s2}$ are the work function and average surface states of the positive and negative tribo-layer, respectively, e is the elementary charge, ε_0 is air permittivity, and x_0 is the separation distance. Due to the increased differences in work function and surface states of the negative tribo-layer (i.e., N_{s2}), Eq. (1) shows how the tribo-charge density can clearly be boosted. It is important to note that TBTO has a higher dipole moment than CBTO which is non-piezoelectric. Thus, it can be expected to promote higher crystallinity and better dipole alignment similarly to how high dipole solvents have been shown to increase crystallinity and dipole alignment for P(VDF-TrFE) [54]. Thus, in the case of P(VDF-TrFE)-TBTO, the Fermi level of the negative triboelectric material can be expected to further shift to a lower level due to a higher surface potential. Thus, this case is expected to show the largest transfer of electrons between the two materials. This appears to be borne out in the TENG electrical output (Fig. 2) and the tribocharge transfer result in Fig. S6 where the TBTO composite gives the highest output. The effect of polarized dipoles in affecting the output performance of Fe-TENGs is illustrated schematically in Fig. 2(a–c). Bound charges are more randomly orientated for P(VDF-TrFE), but become more biased towards a positive charge directed towards the surface as we move to P(VDF-TrFE)/CBTO and P(VDF-TrFE)/TBTO, thereby attracting more electrons from the countersurface (i.e. more surface tribocharges). Since P(VDF-TrFE)/TBTO is ferroelectrically optimum here (as explained above due to higher amount and crystallinity of β-phase etc.), the schematic shows the greatest bias of bound charges and highest density of tribo-charges for the TBTO case.

To investigate the contribution of conventional piezoelectricity to the TENG output, we tested a P(VDF-TrFE)/TBTO device in piezoelectric mode only. The result is shown in Fig. S4 in Supplementary Information. Here we see that output voltage (1.25 V) at max contact force (8 N) is less than 1% of the corresponding output (315 V) in TENG mode (see Fig. 2d). Thus, the TENG devices in this work are referred to as ferroelectric assisted TENGs rather than hybrid TENGs as the piezoelectric contribution can be considered relatively insignificant. All the above effects (increased permittivity and higher surface polarization) essentially combine in the case of the electrospun P(VDF-TrFE)-TBTO NFs to boost tribo-charge density and deliver the best output performance in the Fe-TENGs device (Fig. 2).

3.2. *Pressure sensitivity, topography and contact area*

We turn now to some other key factors that affect the output of these ferroelectric-assisted NF based TENGs. We know that TENG output is generally sensitive to contact pressure for TENGs having solid rough surfaces [27,28]. Fig. 5 shows that this is also the case for the fibrous P(VDF-TrFE) matrix in contact with PET here. At this low-pressure range (3.2–12.8 kPa), we observe a roughly linear increase of voltage with pressure. The calculated pressure sensitivities (S) for pristine P(VDF-TrFE), P(VDF-TrFE)/CBTO and P(VDF-TrFE)/TBTO are 27, 28, and 32 V/kPa, respectively. Interestingly, the obtained sensitivity value for P(VDF-TrFE)/TBTO (S = 32 V/kPa) is higher than previously

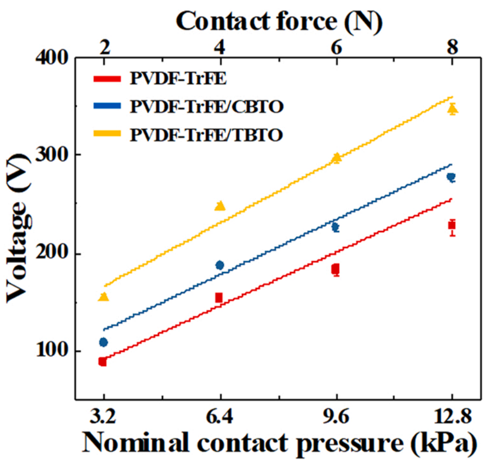

Fig. 5. Open circuit voltage versus nominal contact pressure.

reported for TENG-based pressure sensors [66]. As expected, the P(VDF-TrFE)/TBTO plot shows higher voltages than P(VDF-TrFE)/CBTO and the P(VDF-TrFE)-CBTO plot gives higher voltages than the pristine P(VDF-TrFE) case.

We know that contact area also affects TENG output [27,28] via the contact pressure and, although the contact pressure was fixed at 12.8 kPa for the electrical results in Fig. 2, it is still possible that differences in the topography or elasticity of the fibrous (electrospun) surfaces could be responsible for the differences in output already discussed. To evaluate this prospect, we imaged the topography of each surface type and used the boundary element method to estimate the real contact area. The topographies of all three P(VDF-TrFE) based nanofiber mats were measured using an optical profilometer (Infinite Focus, Alicona) prior to testing and the surface roughness of the PET film was measured by Atomic Force Microscopy (AFM, Bruker, US). The roughness height contours of pure P(VDF-TrFE), P(VDF-TrFE)/CBTO and P(VDF-TrFE)/TBTO NF mats are shown in Fig. 6a–c, respectively and the corresponding height contour plot is shown for the PET countersurface in Fig. S11. The root mean square roughness (Sq) of the three types of P(VDF-TrFE) mats and the PET film are given in Table 2. It is nearly impossible to optically measure the real contact area between these two thin layers using the current test rig, thus, the boundary element method (BEM) [67] is utilized to simulate the linear elastic quasi-static contact between PET and each of the three types of P(VDF-TrFE) based NF mat. Since the sampling area (0.5 × 0.7 mm^2)

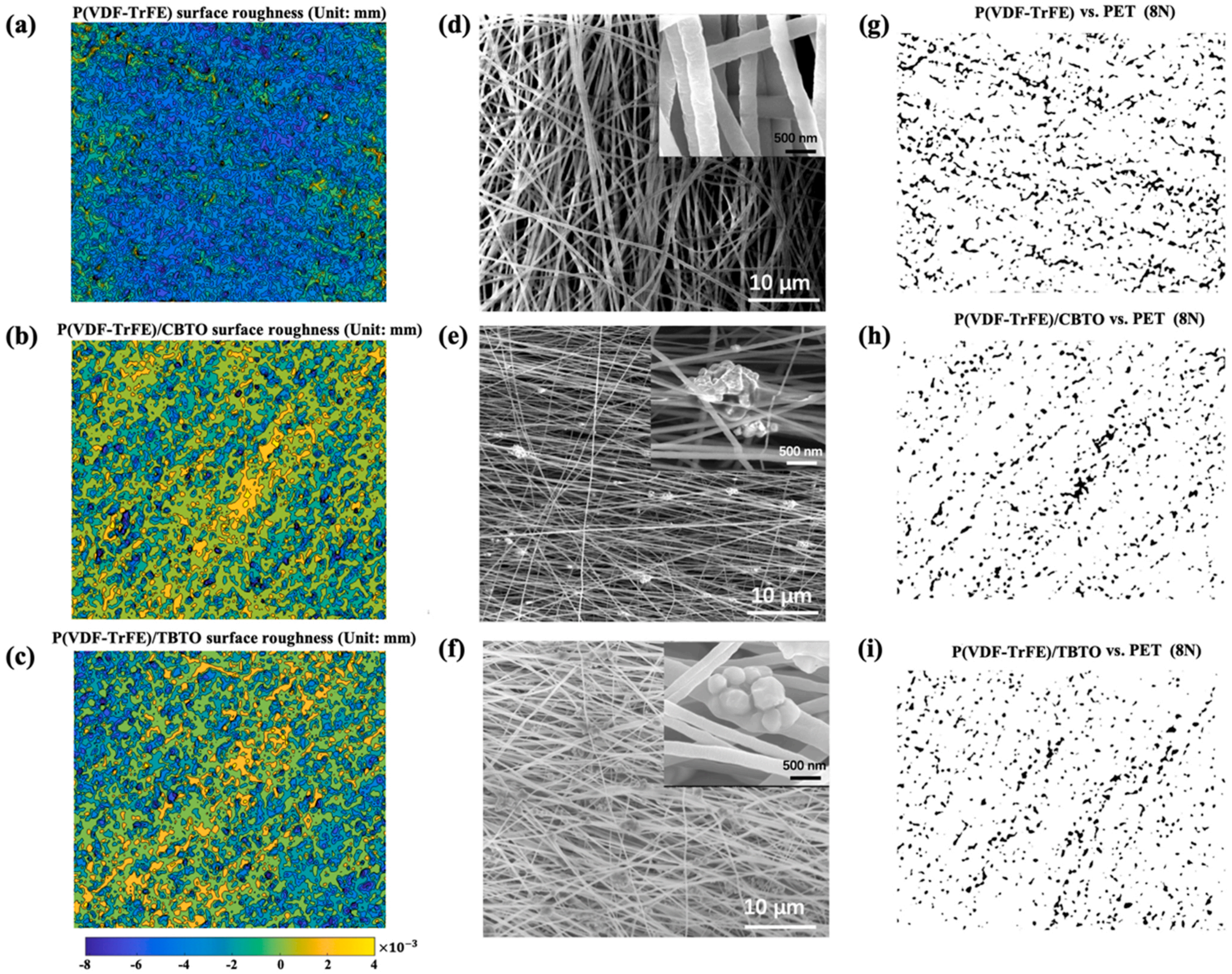

Fig. 6. Surface topography and contact analysis: surface height contour plots of (a) P(VDF-TrFE), (b) P(VDF-TrFE)/CBTO and (c) P(VDF-TrFE)/TBTO. SEM images of nanofiber surfaces for (d) P(VDF-TrFE), (e) P(VDF-TrFE)/CBTO and (f) P(VDF-TrFE)/TBTO (inset images at higher magnification). BEM prediction of real contact area (in black) for: (g) P(VDF-TrFE) & PET, (h) P(VDF-TrFE)/CBTO & PET and (i) P(VDF-TrFE)/TBTO & PET. Note how the predicted contact area follows the peaks of the fibers in the fiber orientation.

Table 2
Areal root mean square surface roughness of the tribo-contact surfaces and predicted contact area percentage (BEM) of the Fe-TENGs tribo-contact pair.

Negative tribo-layer	RMS roughness (Sq) (μm)	Average contact area percentage ($A_r/A_n \times 100$)	Positive tribo-layer (PET sheet) RMS roughness (Sq) (nm)
P(VDF-TrFE)	0.57	10.8%	9.5
P(VDF-TrFE)/CBTO	1.7	6.7%	9.5
P(VDF-TrFE)/TBTO	1.8	5.6%	9.5

measured by the optical profilometer is much smaller than the nominal contact area of the TENG devices ($25 \times 25\ mm^2$), the periodic assumption is adopted in the BEM assuming that the sampling area is periodic along two orthogonal scanning directions. Since the Sq of the PET film is approximately 143 times smaller than the average Sq of all three P(VDF-TrFE) NF mats (see Table 2), the rough surface contact simulation can be simplified to a rough-on-flat scenario. Note, the roughness of the positive tribo-layer was fixed by reusing the PET sheet. The surface morphology of the electrospun nanofibers for the three cases of tribo-negative layers were characterized using the SEM and are shown in Fig. 6d–f. Each of the three types of NF mats exhibited a completely fibrous structure with uniform distribution of nanofibers and an average fiber diameter of 250 nm. As shown in Fig. 6e and f, the BTO nanoparticles are inserted into the nanofibers uniformly and particles can be seen on the surface of the fibers. We see from Table 2 that the mats with the BTO particles have higher Sq roughness (1.7 and 1.8 μm) than the pristine case (0.57 μm). The BEM results for real contact area on the Fe-TENGs interfaces (at 12.8 kPa) are illustrated in Fig. 6g–i in the form of binary images where black pixels represent contact area. The binary images indicate that: (1) the contact commonly occurs on the higher peaks of the PVDF mats and its composites and, (2) the contact area distributions reflect the orientations of the clusters of high peaks on the rough surfaces. The total real contact area (A_r) is simply the sum of the black areas and the contact area ratio is defined as A_r/A_n where A_n is the (total) sampling area of the rough surface. The BEM calculation for each device is repeated three times using three different rough surface data measurements at different locations over the same P(VDF-TrFE) based NF mats. The BEM predicts a contact area ratio of 10.8% for P(VDF-TrFE), 6.7% for P(VDF-TrFE)/CBTO and 5.6% for P(VDF-TrFE)/TBTO. This corresponds with the surface roughness trend – i.e., the rougher the surfaces, the lesser the contact area. Considering the electrical outputs now, we note that, although the contact area prediction is highest for pristine P(VDF-TrFE), electrical output is lowest for this case. Also, electrical output is significantly higher for P(VDF-TrFE)-TBTO compared to P(VDF-TrFE) but this is not the case for the predicted real contact areas which were similar (TBTO actually predicting a slightly lower contact area). Thus, we can rule out contact area as an explanation for the trends already observed in the results based on all devices based on fibrous electro-negative material.

3.3. *Ferroelectric-assisted TENG powered high performance self-charging system*

Finally, the ability of the best performing Fe-TENGs (i.e., P(VDF-TrFE)/TBTO & PET) to charge an integrated supercapacitor was investigated. The purpose of demonstrating charging of the supercapacitor with the Fe-TENG device is to show its self-charging ability for applications like wearable electronics. In such applications, a supercapacitor is more suitable compared to a common electrolytic capacitor due to its very high energy density, flexibility, and ease of integration. A graphene sheet (GS) based flexible supercapacitor (FSC) [51] with PVA-H_3PO_4 gel electrolyte was used as shown in Fig. 7a. The electronic circuit which connects it with the Fe-TENGs via a rectifier is shown in Fig. 7b. In the self-charging system, the Fe-TENGs will generate the free charges which are stored in the graphene sheet supercapacitor (GSC) through the rectifier. The purpose of the rectifier is to convert the alternating current (AC) output of the Fe-TENGs (see Fig. 2d,e) to direct current (DC) and hence provide a continuous electrical power supply to store the energy into the GSC. Fig. 7c shows rapid charging (~5 min) of the GSC with the Fe-TENGs under different applied forces with a fixed vibration time (5 min) and frequency (8 Hz) followed by a slower self-discharging. It is evident from Fig. 7c that with increase in contact forces between 2 and 8 N (i.e., 3.2–12.8 kPa), the maximum output voltage of the SC also increased roughly linearly. This is further evident from Fig. 7d which shows the variation in maximum output voltage with nominal contact pressures (i.e., contact force/nominal area). It was observed that the voltage could be improved from 0.75 V to 1 V, when the contact pressure increased from 3.2 to 12.8 kPa. A similar observation can also be seen in Fig. 7e and f, when the operation frequencies varied between 2 and 10 Hz at a fixed time (5 min) and contact pressure 12.8 kPa (8 N) – i.e., the output voltage also increases roughly linearly with frequency. This is due to the increased output current with increasing TENG operating frequency [68] which can be calculated as:

$$I = \frac{dQ}{dt} \tag{2}$$

Where, Q is output charge and t is generation period. To increase confidence in the results, three GSC devices with near identical specifications were fabricated and the experiments repeated, with results shown in Fig. 7d and f. Note that the error in Fig. 7d and f is due to expected variation between the three separately fabricated GSC devices rather than instability in a single device.

Table 3 summarizes the performance of the present device with the related TENG based self-charging supercapacitor systems in the literature. In the present work, we could charge the GSC to 1.25 V voltage within the short time period of about 5 min. This is a considerably lower charging time then the other TENG based supercapacitor systems in Table 3 which vary from 20 to 180 min, thus showing the compatibility of presented devices as an excellent energy harvesting and storage system. For instance, the Polypyrrole paper-based SC charged by a TENG interface pair of PPy/Cellulose paper and Nitrocellulose membrane exhibited a maximum charged voltage value of 1.5 V in 167 min at a frequency of 10 Hz (similar to this work) and under much higher contact pressure of 30 kPa [69]. In the present work, we were able to charge the SC in a considerably lower charging time and much lower contact pressure, thus indicating the high efficiency of the self-charging system. The rapid charge time is due to high electron mobility in the graphene electrodes which reduce SC impedance as well as the high current being produced by the Fe-TENGs. However, during the self-discharging of the GSC, a rapid drop in voltage to about 0.4 V, followed by a slow decrease, is apparent (Fig. 7c and e). This high drift in potential or fast discharging indicates the low efficiency of charge storing capacity of the graphene electrode. This is because of the low electroactive surface area, low electrochemical activity and hydrophobicity of graphene electrodes [51]. However, this may still be sufficient for wearable applications as often low power sensors (nanowatt to microwatt power range [70–73]) are needed to be powered. We have also demonstrated the charging of three series connected GSCs to a maximum 2.3 V voltage with the presented Fe-TENG devices (see Video 1 in Supplementary Information). To demonstrate the high energy harvesting efficiency of the Fe-TENGs supercapacitor system, we have lighted 40 LEDs connected in series forming the word 'BEST' as shown in Fig. 7g. In this case, the applied contact pressure was 0.8 kPa at a frequency of 8 Hz. Video 2 in Supplementary Information illustrates how the LEDs are bright even at this low contact pressure. Hence the Fe-TENGs/supercapacitor system produces usable output even at low contact pressures such as those available in wearable applications.

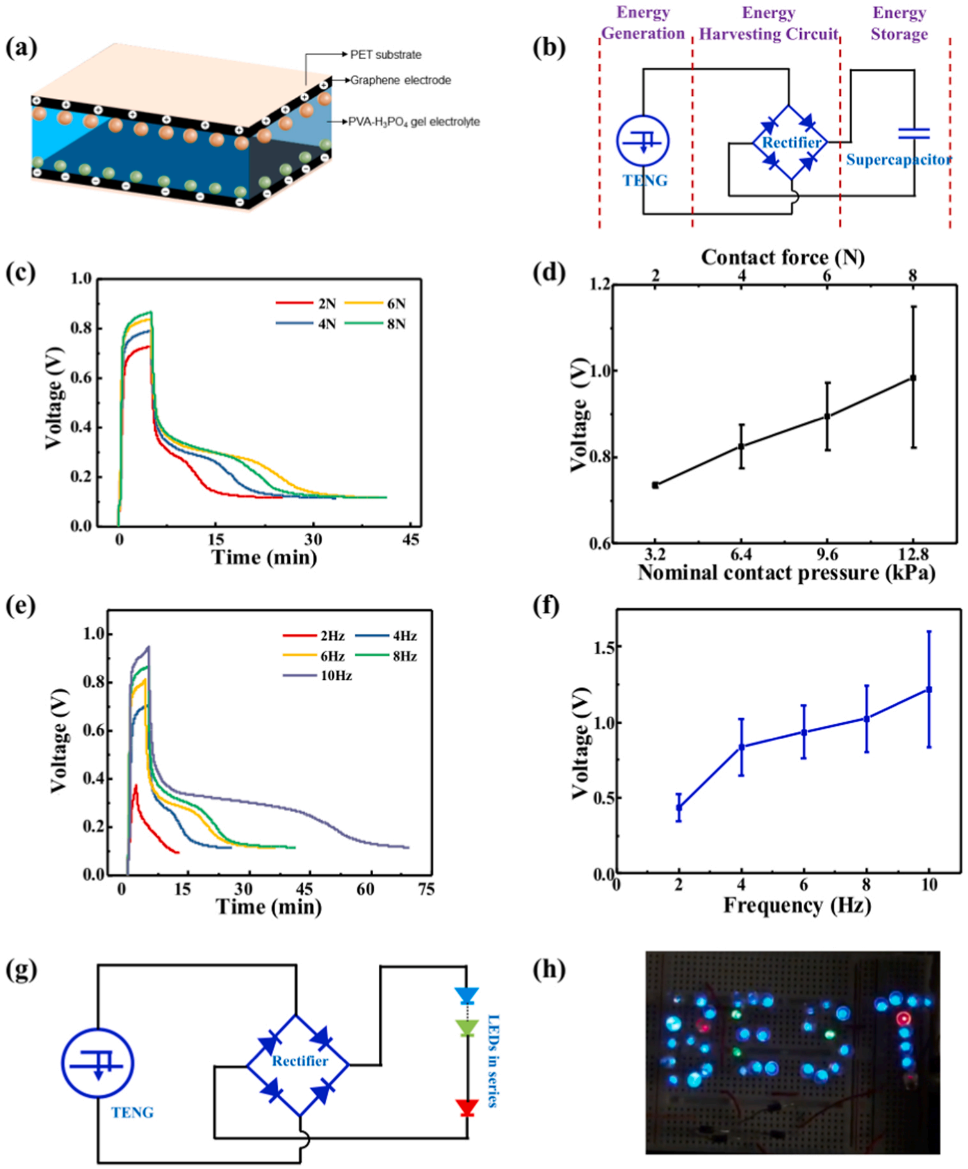

Fig. 7. (a) Schematic of graphene electrode based flexible supercapacitor (SC), (b) energy harvesting circuit for self-charging system (i.e. integration with the Fe-TENGs), (c) charging and discharging voltage of SC at different contact forces (frequency of 8 Hz), (d) the maximum value of voltage charge into the SC versus nominal contact pressure, (e) charging and discharging voltage of SC by different frequencies (contact pressure 12.8 kPa), (f) the maximum value of voltage charge into the SC versus vibration frequencies, (g) representative energy harvesting circuit of Fe-TENGs for lighting LEDs and (h) photograph of lighted LED array representing the word "BEST".

Table 3

Typical charging performance and charging period for TENG based self-charging systems in the literature as compared with the present work (final row).

TENG interface pair	SC electrode & electrolytes	Pressure (kPa)	Frequency (Hz)	Period (min)	$V_{max\ ,\ SC}$ (V)	Ref.
C_4F_8 & ITO	Electrode: CNT/paper Electrolytes: PVA/H_3PO_4	-	8	180	0.9	[74]
PTFE & ITO	Electrode: Cu sheet Electrolytes: [BMIM] [BF4]/ ETPTA	40	2	20	0.06	[75]
LIG & PTFE	Electrode: LIG Electrolytes: PVA/H_2PO_4	-	-	117	3	[76]
PTFE & Al	Electrode: peptide-Co_9S_8 Electrolytes: KOH/PVA	-	1	167	1.78	[77]
PVDF-HFP & steel	Electrode: $CoFe_2O_4$ and Fe-RGO Electrolytes: Fe^{3+}-PAA/KOH	44	3.8	32	1.6	[78]
PPy/Cellulose paper & Nitrocellulose Membrane	Electrode: Polypyrrole Electrolytes: PVA/H_3PO_4	30	10	167	1.5	[69]
P(VDF-TrFE)/TBTO NFs & PET	Electrode: Graphene Electrolytes: PVA/H_3PO_4	12.8	10	5	1.25	This work

4. Conclusions

In this paper, novel ferroelectric-assisted TENGs (Fe-TENGs) are fabricated whereby the tribo-negative surface is based on electrospun P(VDF-TrFE) composite nano-fibrous mats (having the advantageous β-phase) with dispersed $BaTiO_3$ (BTO) nanofillers in either cubic (CBTO) or tetragonal (TBTO) form. The approach uses electrospinning to significantly increase triboelectric output by boosting surface polarization. TENGs with three types of tribo-negative surface were investigated: pristine P(VDF-TrFE), P(VDF-TrFE)/CBTO and P(VDF-TrFE)/TBTO. The tribo-positive surface was smooth PET. Open circuit voltage and short circuit current density increased progressively from the pristine P(VDF-TrFE) case (225 V & 1.9 μA/cm^2) to P(VDF-TrFE)/CBTO (293 V & 5.5 μA/cm^2) and reached a maximum for P(VDF-TrFE)/TBTO (315 V & 6.7 μA/cm^2), representing 1.4 and 3.4 times increase in voltage and current density, respectively. The corresponding optimum power densities were 0.75, 2 and 2.75 W/m^2, respectively. Accounting for contact pressure, max output (V_{oc} = 315 V & J_{sc} = 6.7 μA/cm^2) is significantly higher than for TENGs having spin-coated P(VDF-TrFE)/BTO. The gain (versus spin-coating and poling) is likely due to enhanced dipole alignment in the P(VDF-TrFE) matrix owing to the higher applied voltage during electrospinning. Also, uniaxial fiber stretching during electrospinning is likely to produce highly aligned, more crystalline P(VDF-TrFE). These effects are likely to confer higher surface polarity (i.e., higher surface potential). The increase in electrical output with the addition of the BTO particles is partly due to these high permittivity particles boosting the permittivity of the P(VDF-TrFE) as has been noted in previous literature. However, we found a significant output increase in moving from P(VDF-TrFE)/CBTO to P(VDF-TrFE)/TBTO even though these two materials have near identical permittivity. XRD and FTIR Spectroscopy analysis have revealed that TENG output is boosted by enhancing the amount and crystallinity of the β-phase of the P(VDF-TrFE) matrix. Higher crystallinity in the β-phase is likely to further increase dipole alignment and further boost surface potential. The overlapped electron cloud (OEC) model explains how this can then boost TENG performance: higher surface potential increases the energy gap between Fermi levels and thereby increases the amount of tribo-charge transfer. Thus, we show that the addition of BTO particles boosts TENG output, not just by enhancing permittivity, but by enhancing the crystallinity and amount of the P(VDF-TrFE)/BTO matrix – hence the higher output with TBTO. Finally, we have developed an efficient self-charging system by integrating the Fe-TENGs with a graphene electrode based flexible supercapacitor. The system is capable of charging to 1.25 V in the notably short time of 5 min due to high electron mobility in the graphene electrodes and high current output from the Fe-TENGs. This technology can have significant application in wearable electronics where higher output currents and more efficient charging are required from devices.

CRediT authorship contribution statement

Guanbo Min: Investigation, Methodology, Software, Validation, Formal analysis, Visualization, Writing – original draft. **Abhilash Pullanchiyodan**: Methodology, Investigation, Writing – review & editing. **Abhishek Singh Dahiya**: Investigation, Validation, Writing – review & editing. **Ensieh Seyed Hosseini**: Investigation, Writing – review & editing. **Yang Xu**: Investigation, Software, Formal analysis, Writing – review & editing. **Daniel Mulvihill**: Supervision, Conceptualization, Writing – review & editing, Project administration, Funding acquisition. **Ravinder Dahiya**: Conceptualization, Supervision, Formal analysis, Resources, Writing – review & editing, Funding acquisition, Project administration.

Declaration of Competing Interest

The authors declare that they have no known competing financial interests or personal relationships that could have appeared to influence the work reported in this paper.

Acknowledgements

The work was supported by the Engineering and Physical Sciences Research Council (EPSRC) through Engineering Fellowship for Growth (EP/R029644/1). This work is also supported in part by a Taiho Kogyo Tribology Research Foundation (TTRF) ‘Research Grant’ entitled “Tribology of Triboelectric Nanogenerators: Understanding how Interface Mechanics effects Electrical Output”. The authors would like to acknowledge the support of the members of the Bendable Electronics and Sensing Technologies (BEST) Group at the University of Glasgow (especially Drs. Saoirse Dervin, Adamos Christou & Gaurav Khandelwal) and Dr. Mario Gonzalez Jimenez from the School of Chemistry for assistance with the FTIR measurements.

Appendix A. Supporting information

Supplementary data associated with this article can be found in the online version at doi:10.1016/j.nanoen.2021.106600.

References

[1] R. Mukherjee, P. Ganguli, R. Dahiya, Bioinspired distributed energy in robotics and enabling technologies, Adv. Intell. Syst. (2021), 2100036.

[2] L. Manjakkal, L. Yin, A. Nathan, J. Wang, R. Dahiya, Energy autonomous sweat-based wearable systems, Adv. Mater. 33 (2021), 2100899.

[3] C. García Núñez, L. Manjakkal, R. Dahiya, Energy autonomous electronic skin, npj Flex. Electron. 3 (2019) 1.

[4] Y. Wang, Y. Yang, Z.L. Wang, High-performance flexible BiCMOS electronics based on single-crystal Si nanomembrane, npj Flex. Electron. 1 (2017) 1–10.

[5] K. Dong, X. Peng, Z.L. Wang, Fiber/fabric-based piezoelectric and triboelectric nanogenerators for flexible/stretchable and wearable electronics and artificial intelligence, Adv. Mater. 32 (2020), 1902549.

[6] T. Huang, Y. Zhang, P. He, G. Wang, X. Xia, G. Ding, T.H. Tao, Self-matched" tribo/piezoelectric nanogenerators using vapor-induced phase-separated poly(vinylidene fluoride) and recombinant spider silk, Adv. Mater. 32 (2020), 1907336.

[7] J. Chen, H. Guo, Z. Wu, G. Xu, Y. Zi, C. Hu, Z.L. Wang, Actuation and sensor integrated self-powered cantilever system based on TENG technology, Nano Energy 64 (2019), 103920.

[8] H. Guo, J. Chen, L. Wang, A.C. Wang, Y. Li, C. An, J.-H. He, C. Hu, V.K.S. Hsiao, Z. L. Wang, A highly efficient triboelectric negative air ion generator, Nat. Sustain. 4 (2021) 147–153.

[9] Y. Su, G. Chen, C. Chen, Q. Gong, G. Xie, M. Yao, H. Tai, Y. Jiang, J. Chen, Self-powered respiration monitoring enabled by a triboelectric nanogenerator, Adv. Mater. 33 (2021), 2101262.

[10] Y. Su, C. Chen, H. Pan, Y. Yang, G. Chen, X. Zhao, W. Li, Q. Gong, G. Xie, Y. Zhou, S. Zhang, H. Tai, Y. Jiang, J. Chen, Muscle fibers inspired high-performance piezoelectric textiles for wearable physiological monitoring, Adv. Funct. Mater. 31 (2021), 2010962.

[11] Y. Su, J. Wang, B. Wang, T. Yang, B. Yang, G. Xie, Y. Zhou, S. Zhang, H. Tai, Z. Cai, G. Chen, Y. Jiang, L.-Q. Chen, J. Chen, Alveolus-inspired active membrane sensors for self-powered wearable chemical sensing and breath analysis, ACS Nano 14 (2020) 6067–6075.

[12] Y. Su, T. Yang, X. Zhao, Z. Cai, G. Chen, M. Yao, K. Chen, M. Bick, J. Wang, S. Li, G. Xie, H. Tai, X. Du, Y. Jiang, J. Chen, A wireless energy transmission enabled wearable active acetone biosensor for non-invasive prediabetes diagnosis, Nano Energy 74 (2020), 104941.

[13] Y. Su, G. Xie, H. Tai, S. Li, B. Yang, S. Wang, Q. Zhang, H. Du, H. Zhang, X. Du, Y. Jiang, Self-powered room temperature NO_2 detection driven by triboelectric nanogenerator under UV illumination, Nano Energy 47 (2018) 316–324.

[14] S. Wang, Y. Jiang, H. Tai, B. Liu, Z. Duan, Z. Yuan, H. Pan, G. Xie, X. Du, Y. Su, An integrated flexible self-powered wearable respiration sensor, Nano Energy 63 (2019), 103829.

[15] Y. Su, M. Yao, G. Xie, H. Pan, H. Yuan, M. Yang, H. Tai, X. Du, Y. Jiang, Improving sensitivity of self-powered room temperature NO_2 sensor by triboelectric-photoelectric coupling effect, Appl. Phys. Lett. 115 (2019), 073504.

[16] Z. Wang, L. Lin, S. Niu, Y. Zi, Triboelectric Nanogenerators, Springer, 2016.

[17] G. Min, L. Manjakkal, D.M. Mulvihill, R.S. Dahiya, Triboelectric nanogenerator with enhanced performance via an optimized low permittivity substrate, IEEE Sens. J. 20 (2019) 6856–6862.

[18] J. Chen, J. Yang, Z. Li, X. Fan, Y. Zi, Q. Jing, H. Guo, Z. Wen, K.C. Pradel, S. Niu, Networks of triboelectric nanogenerators for harvesting water wave energy: a potential approach toward blue energy, ACS nano 9 (2015) 3324–3331.

[19] B. Chen, Y. Yang, Z.L. Wang, Scavenging wind energy by triboelectric nanogenerators, Adv. Energy Mater. 8 (2018), 1702649.

[20] J. Chen, H. Guo, C. Hu, Z.L. Wang, Robust triboelectric nanogenerator achieved by centrifugal force induced automatic working mode transition, Adv. Energy Mater. 10 (2020), 2000886.

[21] F.-R. Fan, Z.-Q. Tian, Z.L. Wang, Flexible triboelectric generator, Nano Energy 1 (2012) 328–334.

[22] S. Wang, L. Lin, Z.L. Wang, Triboelectric nanogenerators as self-powered active sensors, Nano Energy 11 (2015) 436–462.

[23] T.X. Xiao, X. Liang, T. Jiang, L. Xu, J.J. Shao, J.H. Nie, Y. Bai, W. Zhong, Z.L. Wang, Spherical triboelectric nanogenerators based on spring-assisted multilayered structure for efficient water wave energy harvesting, Adv. Funct. Mater. 28 (2018), 1802634.

[24] Y.H. Kwon, S.-H. Shin, J.-Y. Jung, J. Nah, Scalable and enhanced triboelectric output power generation by surface functionalized nanoimprint patterns, Nanotechnology 27 (2016), 205401.

[25] W. Liu, Z. Wang, G. Wang, G. Liu, J. Chen, X. Pu, Y. Xi, X. Wang, H. Guo, C. Hu, Z. L. Wang, Integrated charge excitation triboelectric nanogenerator, Nat. Commun. 10 (2019) 1426.

[26] Z. Wang, W. Liu, W. He, H. Guo, L. Long, Y. Xi, X. Wang, A. Liu, C. Hu, Ultrahigh electricity generation from low-frequency mechanical energy by efficient energy management, Joule 5 (2021) 441–455.

[27] Y. Xu, G. Min, N. Gadegaard, R. Dahiya, D.M. Mulvihill, A unified contact force-dependent model for triboelectric nanogenerators accounting for surface roughness, Nano Energy 76 (2020), 105067.

[28] G. Min, Y. Xu, P. Cochran, N. Gadegaard, D.M. Mulvihill, R. Dahiya, Origin of the contact force-dependent response of triboelectric nanogenerators, Nano Energy 83 (2021), 105829.

[29] X. He, H. Guo, X. Yue, J. Gao, Y. Xi, C. Hu, Improving energy conversion efficiency for triboelectric nanogenerator with capacitor structure by maximizing surface charge density, Nanoscale 7 (2015) 1896–1903.

[30] J. Chen, H. Guo, X. He, G. Liu, Y. Xi, H. Shi, C. Hu, Enhancing performance of triboelectric nanogenerator by filling high dielectric nanoparticles into sponge PDMS film, ACS Appl. Mater. Interfaces 8 (2016) 736–744.

[31] Y.J. Kim, J. Lee, S. Park, C. Park, C. Park, H.-J. Choi, Effect of the relative permittivity of oxides on the performance of triboelectric nanogenerators, RSC Adv. 7 (2017) 49368–49373.

[32] Y. Park, Y.-E. Shin, J. Park, Y. Lee, M.P. Kim, Y.-R. Kim, S. Na, S.K. Ghosh, H. Ko, Ferroelectric multilayer nanocomposites with polarization and stress concentration structures for enhanced triboelectric performances, ACS nano 14 (2020) 7101–7110.

[33] J.S.C. Koay, W.C. Gan, A.E. Soh, J.Y. Cheong, K.C. Aw, T.S. Velayutham, An overlapped electron-cloud model for the contact electrification in piezo-assisted triboelectric nanogeneratorsviacontrol of piezoelectric polarization, J. Mater. Chem. A 8 (2020) 25857–25866.

[34] Y.Z. Liu, H. Zhang, J.X. Yu, Z.Y. Huang, C. Wang, Y. Sun, Ferroelectric P(VDF-TrFE)/POSS nanocomposite films: compatibility, piezoelectricity, energy harvesting performance, and mechanical and atomic oxygen erosion, RSC Adv. 10 (2020) 17377–17386.

[35] X. Ma, S. Li, S. Dong, J. Nie, M. Iwamoto, S. Lin, L. Zheng, X. Chen, Regulating the output performance of triboelectric nanogenerator by using P(VDF-TrFE) Langmuir monolayers, Nano Energy 66 (2019), 104090.

[36] X. Tao, H. Jin, M. Ma, L. Quan, J. Chen, S. Dong, H. Zhang, C. Lv, Y. Fu, J. Luo, Significantly enhanced performance of triboelectric nanogenerator by incorporating $BaTiO_3$ nanoparticles in poly(vinylidene fluoride) film, Phys. Status Solidi A 216 (2019) 1900068.

[37] H.-S. Kim, I.-K. Park, Enhanced output power from triboelectric nanogenerators based on electrospun Eu-doped polyvinylidene fluoride nanofibers, J. Phys. Chem. Solids 117 (2018) 188–193.

[38] Y. Wu, J. Qu, W.A. Daoud, L. Wang, T. Qi, Flexible composite-nanofiber based piezo-triboelectric nanogenerators for wearable electronics, J. Mater. Chem. A 7 (2019) 13347–13355.

[39] S. Cheon, H. Kang, H. Kim, Y. Son, J.Y. Lee, H.-J. Shin, S.-W. Kim, J.H. Cho, High-performance triboelectric nanogenerators based on electrospun polyvinylidene fluoride-silver nanowire composite nanofibers, Adv. Funct. Mater. 28 (2018), 1703778.

[40] H.-Y. Mi, X. Jing, Q. Zheng, L. Fang, H.-X. Huang, L.-S. Turng, S. Gong, High-performance flexible triboelectric nanogenerator based on porous aerogels and electrospun nanofibers for energy harvesting and sensitive self-powered sensing, Nano Energy 48 (2018) 327–336.

[41] Y. Guo, X.-S. Zhang, Y. Wang, W. Gong, Q. Zhang, H. Wang, J. Brugger, All-fiber hybrid piezoelectric-enhanced triboelectric nanogenerator for wearable gesture monitoring, Nano Energy 48 (2018) 152–160.

[42] T. Bhatta, P. Maharjan, H. Cho, C. Park, S.H. Yoon, S. Sharma, M. Salauddin, M. T. Rahman, S.M.S. Rana, J.Y. Park, High-performance triboelectric nanogenerator based on MXene functionalized polyvinylidene fluoride composite nanofibers, Nano Energy 81 (2021), 105670.

[43] L. Shi, H. Jin, S. Dong, S. Huang, H. Kuang, H. Xu, J. Chen, W. Xuan, S. Zhang, S. Li, X. Wang, J. Luo, High-performance triboelectric nanogenerator based on electrospun PVDF-graphene nanosheet composite nanofibers for energy harvesting, Nano Energy 80 (2021), 105599.

[44] S.M.S. Rana, M.T. Rahman, M. Salauddin, S. Sharma, P. Maharjan, T. Bhatta, H. Cho, C. Park, J.Y. Park, Electrospun PVDF-TrFE/MXene nanofiber mat-based triboelectric nanogenerator for smart home appliances, ACS Appl. Mater. Interfaces 13 (2021) 4955–4967.

[45] S. Ma, T. Ye, T. Zhang, Z. Wang, K. Li, M. Chen, J. Zhang, Z. Wang, S. Ramakrishna, L. Wei, Highly oriented electrospun P(VDF-TrFE) fibers via mechanical stretching for wearable motion sensing, Adv. Mater. Technol. 3 (2018), 1800033.

[46] Y. Su, W. Li, L. Yuan, C. Chen, H. Pan, G. Xie, G. Conta, S. Ferrier, X. Zhao, G. Chen, H. Tai, Y. Jiang, J. Chen, Piezoelectric fiber composites with polydopamine interfacial layer for self-powered wearable biomonitoring, Nano Energy 89 (2021), 106321.

[47] W. Seung, H.-J. Yoon, T.Y. Kim, H. Ryu, J. Kim, J.-H. Lee, J.H. Lee, S. Kim, Y. K. Park, Y.J. Park, S.-W. Kim, Boosting power-generating performance of triboelectric nanogenerators via artificial control of ferroelectric polarization and dielectric properties, Adv. Energy Mater. 7 (2017), 1600988.

[48] D. Ali, B. Yu, X. Duan, H. Yu, M. Zhu, Enhancement of output performance through post-poling technique on BaTiO3/PDMS-based triboelectric nanogenerator, Nanotechnology 28 (2017), 075203.

[49] H. Patnam, B. Dudem, S.A. Graham, J.S. Yu, High-performance and robust triboelectric nanogenerators based on optimal microstructured poly(vinyl alcohol) and poly(vinylidene fluoride) polymers for self-powered electronic applications, Energy 223 (2021), 120031.

[50] S.S.K. Mallineni, H. Behlow, R. Podila, A.M. Rao, A low-cost approach for measuring electrical load currents in triboelectric nanogenerators, Nanotechnol. Rev. 7 (2018) 149–156.

[51] L. Manjakkal, W.T. Navaraj, C.G. Núñez, R. Dahiya, Graphene–graphite polyurethane composite based high-energy density flexible supercapacitors, Adv. Sci. 6 (2019), 1802251.

[52] A. Pullanchiyodan, L. Manjakkal, S. Dervin, D. Shakthivel, R. Dahiya, Metal coated conductive fabrics with graphite electrodes and biocompatible gel electrolyte for wearable supercapacitors, Adv. Mater. Technol. 5 (2020), 1901107.

[53] P. Bai, G. Zhu, Y.S. Zhou, S. Wang, J. Ma, G. Zhang, Z.L. Wang, Dipole-moment-induced effect on contact electrification for triboelectric nanogenerators, Nano Res. 7 (2014) 990–997.

[54] J. Kim, J.H. Lee, H. Ryu, J.-H. Lee, U. Khan, H. Kim, S.S. Kwak, S.-W. Kim, High-performance piezoelectric, pyroelectric and triboelectric nanogenerator based on PVDF-TrFE with controlled crystallinity and dipole alignment, Adv. Funct. Mater. 27 (2017) 1700702.

[55] P. Martins, A. Lopes, S. Lanceros-Mendez, Electroactive phases of poly(vinylidene fluoride): determination, processing and applications, Prog. Polym. Sci. 39 (2014) 683–706.

[56] E.S. Hosseini, L. Manjakkal, D. Shakthivel, R. Dahiya, Glycine-chitosan-based flexible biodegradable piezoelectric pressure sensor, ACS Appl. Mater. Interfaces 12 (2020) 9008–9016.

[57] D. Yoon, Tetragonality of barium titanate powder for a ceramic capacitor application, J. Ceram. Process. Res. 7 (2006) 343–354.

[58] M. Acosta, N. Novak, V. Rojas, S. Patel, R. Vaish, J. Koruza, G. Rossetti Jr., J. Rödel, $BaTiO_3$-based piezoelectrics: fundamentals, current status, and perspectives, Appl. Phys. Rev. 4 (2017), 041305.

[59] J. Nunes-Pereira, V. Sencadas, V. Correia, V.F. Cardoso, W. Han, J.G. Rocha, S. Lanceros-Méndez, Energy harvesting performance of $BaTiO_3$/poly(vinylidene fluoride–trifluoroethylene) spin coated nanocomposites, Compos. Part B Eng. 72 (2015) 130–136.

[60] X. Hu, X. Yan, L. Gong, F. Wang, Y. Xu, L. Feng, D. Zhang, Y. Jiang, Improved piezoelectric sensing performance of P(VDF-TrFE) nanofibers by utilizing BTO nanoparticles and penetrated electrodes, ACS Appl. Mater. Interfaces 11 (2019) 7379–7386.

[61] A.P. Indolia, M. Gaur, Investigation of structural and thermal characteristics of PVDF/ZnO nanocomposites, J. Therm. Anal. Calorim. 113 (2013) 821–830.

[62] K. Yu, H. Wang, Y. Zhou, Y. Bai, Y. Niu, Enhanced dielectric properties of $BaTiO_3$/poly(vinylidene fluoride) nanocomposites for energy storage applications, J. Appl. Phys. 113 (2013), 034105.

[63] S. Gupta, D. Shakthivel, L. Lorenzelli, R. Dahiya, An environmentally-benign synthesis of spiro-benzo[1,4]diazepines using multi phase nano-titania as a highly efficient catalyst via MAOS technique, IEEE Sens. J. 19 (2019) 435–442.

[64] C. Xu, Y. Zi, A.C. Wang, H. Zou, Y. Dai, X. He, P. Wang, Y.C. Wang, P. Feng, D. Li, On the electron-transfer mechanism in the contact-electrification effect, Adv. Mater. 30 (2018), 1706790.

[65] P. Vasandani, Z.-H. Mao, W. Jia, M. Sun, Relationship between triboelectric charge and contact force for two triboelectric layers, J. Electrost. 90 (2017) 147–152.

[66] X. Pu, M. Liu, X. Chen, J. Sun, C. Du, Y. Zhang, J. Zhai, W. Hu, Z.L. Wang, Ultrastretchable, transparent triboelectric nanogenerator as electronic skin for biomechanical energy harvesting and tactile sensing, Sci. Adv. 3 (2017), e1700015.

[67] I. Polonsky, L. Keer, A numerical method for solving rough contact problems based on the multi-level multi-summation and conjugate gradient techniques, Wear 231 (1999) 206–219.

[68] R.D.I.G. Dharmasena, K. Jayawardena, C. Mills, J. Deane, J. Anguita, R. Dorey, S. Silva, Triboelectric nanogenerators: providing a fundamental framework, Energy Environ. Sci. 10 (2017) 1801–1811.

[69] X. Shi, S. Chen, H. Zhang, J. Jiang, Z. Ma, S. Gong, Portable self-charging power system via integration of a flexible paper-based triboelectric nanogenerator and supercapacitor, ACS Sustain. Chem. Eng. 7 (2019) 18657–18666.

[70] P. Escobedo, M. Ntagios, D. Shakthivel, W.T. Navaraj, R. Dahiya, Mediastinitis of odontogenic origin. A serious complication with 80 years of history, IEEE Trans. Robot. 37 (2) (2021) 683–690.

[71] H. Wang, P.P. Mercier, Near-zero-power temperature sensing via tunneling currents through complementary metal-oxide-semiconductor transistors, Sci. Rep. 7 (2017) 4427.

[72] T. Tekeste, H. Saleh, B. Mohammad, A. Khandoker, H. Jelinek, M. Ismail, A nanowatt real-time cardiac autonomic neuropathy detector, IEEE Trans. Biomed. Circuits Syst. 12 (2018) 739–750.

[73] P. Escobedo, M. Bhattacharjee, F. Nikbakhtnasrabadi, R. Dahiya, Smart bandage with wireless strain and temperature sensors and batteryless NFC tag, IEEE Internet Things J. 8 (6) (2021) 5093–5100.

[74] Y. Song, X. Cheng, H. Chen, J. Huang, X. Chen, M. Han, Z. Su, B. Meng, Z. Song, H. Zhang, Integrated self-charging power unit with flexible supercapacitor and triboelectric nanogenerator, J. Mater. Chem. A 4 (2016) 14298–14306.

[75] J. Zou, M. Zhang, J. Huang, J. Bian, Y. Jie, M. Willander, X. Cao, N. Wang, Z. L. Wang, Coupled Supercapacitor and Triboelectric Nanogenerator Boost, Biomimetic Pressure Sensor 8 (2018) 1702671.

[76] J. Luo, F.R. Fan, T. Jiang, Z. Wang, W. Tang, C. Zhang, M. Liu, G. Cao, Z.L. Wang, Integration of micro-supercapacitors with triboelectric nanogenerators for a flexible self-charging power unit, Nano Res. 8 (2015) 3934–3943.

[77] W. Xiong, K. Hu, Z. Li, Y. Jiang, Z. Li, Z. Li, X. Wang, A wearable system based on core-shell structured peptide-Co9S8 supercapacitor and triboelectric nanogenerator, Nano Energy 66 (2019), 104149.

[78] A. Maitra, S. Paria, S.K. Karan, R. Bera, A. Bera, A.K. Das, S.K. Si, L. Halder, A. De, B.B. Khatua, Triboelectric nanogenerator driven self-charging and self-healing flexible asymmetric supercapacitor power cell for direct power generation, ACS Appl. Mater. Interfaces 11 (2019) 5022–5036.

Guanbo Min received a B.Sc. degree in Electronic Information Technology from Macau University of Science and Technology, Macao S.A.R, China in 2015 and a M.Sc. degree in Electronics and Electrical Engineering from University of Glasgow in 2017. Since 2017, he has been a Ph.D. student in Bendable Electronics and Sensing Technologies (BEST) group at University of Glasgow. His work is focused on optimizing triboelectric nanogenerator performance.

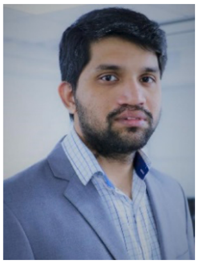

Abhilash Pullanchiyodan received B.Sc. and M.Sc. degree in Chemistry, from Kannur University, Kerala, India, and Ph.D. degree in Chemical Science (Chemistry) in 2018, from Academy of Scientific and Innovative Research (AcSIR), India. From 2018-2021 he worked as a Royal Society-SERB Newton International Fellow in Bendable Electronics and Sensing Technologies (BEST group at University of Glasgow (UK). His research interest includes supercapacitors, nanomaterials, ink/paste formulation, microwave dielectrics and ceramics.

Abhishek S. Dahiya is Research Associate in the Bendable Electronics and Sensing Technologies (BEST) at the University of Glasgow. He received Ph.D. from the GREMAN laboratory, Université François Rabelais de Tours, France in 2016. He has done postdoctoral work at various CNRS laboratories in France: GREMAN (2016-2017), ICMCB (2018-2019), and IES/LIRMM (2019-2020). His research interest includes synthesis of nanomaterials, nanofabrication, energy harvesting, and printed and flexible electronics.

Ensieh Seyed Hosseini obtained her M.Sc. (2011) degree in Chemistry from the Sharif University of Technology in Iran, and Ph.D. (2015) in Nanoscience and Nanotechnology from the University of Aveiro in Portugal. Afterward, she was a postdoctoral researcher in the Bendable Electronics and Sensing Technologies (BEST) at the University of Glasgow and Strathclyde, UK and subsequently she worked at Marie Curie fellow and research associate in BEST group at University of Glasgow. Her research interests are focused on the application of novel functional biomaterials and nanofibers in flexible sensors and energy harvesters.

Yang Xu is a Research Professor in mechanical engineering at Hefei University of Technology. He received his M.S and Ph.D. degrees in mechanical engineering at Auburn University in 2012 and 2017, respectively. From 2018 to 2020, he was a Research Associate at University of Glasgow. He has research interests in the fundamentals of contact mechanics and its applications in the multidisciplinary fields, e.g.,tribology, contact-/tribo-electrification, triboelectric nanogenerator, etc.

Daniel Mulvihill is Senior Lecturer (Associate Professor) in Mechanical Engineering at University of Glasgow. He completed a D.Phil. in Engineering Science at the University of Oxford in 2012 and subsequently undertook postdoctoral periods at the University of Limerick, EPFL Switzerland and the University of Cambridge prior to joining Glasgow in 2016. His interests are mainly focused on materials engineering and tribology. Dr Mulvihill is a former Institution of Mechanical Engineers (IMechE) Tribology Trust Bronze Medalist(2013).

Ravinder Dahiya is Professor of Electronics and Nanoengineering and EPSRC research fellow at the University of Glasgow. He is the leader of Bendable Electronics and Sensing Technologies (BEST) research group, which conducts fundamental and applied research in flexible and printed electronics, tactile sensing, electronic skin, robotics, and energy autonomous systems. He has led several international projects on e-skin, interactive systems, and flexible electronics. He is founding Editor-in-Chief of IEEE Journal on Flexible Electronics (J-FLEX). He is an IEEE Fellow.